ChemPubSoc Europe

DOI: 10.1002/ejic.201900946

EurJIC European Journal of Inorganic Chemistry

Full Paper

Mechanochemistry

Reactive Milling Induced Structure Changes in Phenylphosphonic Acid Functionalized $LiMn_2O_4$ Nanocrystals – Synthesis, Rietveld Refinement, and Thermal Stability

Dennis Becker,[a] Robert Haberkorn,[a] and Guido Kickelbick*[a]

Abstract: Spinel $LiMn_2O_4$ formed in a solid-state reaction was treated with a high energy planetary ball mill. A mechanochemical in situ surface functionalization of the nanocrystallites with a size smaller than 10 nm was achieved by addition of phenylphosphonic acid. The functionalization was proven by infrared spectroscopy and it can be shown that it prevents the formation of Mn_2O_3 during the milling process. Structural changes of the samples were investigated via XRD and Rietveld refinement. Mild milling conditions induce an anisotropic broadening of the reflections caused by a distribution of lattice parameters. In this first stage, we propose a structure model based on orthorhombic $LiMn_2O_4$. DSC and in situ XRD measurements also verify the presence of the orthorhombic low temperature phase. Medium milling conditions induce a change of intensities, correlated to a cation disorder. Harsher milling conditions induce the transformation to a tetragonal phase. The thermal stability of the formed phases was investigated via in situ high temperature XRD. The reformation of cubic spinel is observed in all samples; however, the transition point depends on the previous milling parameters.

1. Introduction

Lithium manganese oxides, especially $LiMn_2O_4$, are well known for their ability to intercalate or deintercalate lithium ions.[1] Based on the reversible lithium intercalation, electrical conductivity, and low cost of manganese, $LiMn_2O_4$ with spinel structure has become a popular cathode material in lithium ion batteries.[2] The typical synthesis of spinel $LiMn_2O_4$ is achieved by a solid-state reaction in air at temperatures above 750 °C, from various oxides or carbonates.[3,4] Coarse-grained materials are obtained in this way. To enhance the electrochemical performance many efforts were carried out to produce nanocrystalline materials to increase the active surface area and decrease the diffusion path lengths.[5] Fine grained or nanocrystalline material can be obtained by lowering the annealing temperature to prevent excessive crystal growth. This may be achieved by dissolving the appropriate metal acetates and complexation agents like citric acid or tartaric acid in ethanol to form a homogeneous precursor powder after drying of the solution.[6,7] Alternatively, metal nitrates and polyvinyl alcohol or ethylene glycol are dissolved in distilled water to obtain a homogeneous precursor powder after drying.[8,9] The disadvantage of these preparation methods is the requirement to use large amounts of solvents and complexations agents, making them less attractive in terms of an environmentally friendly production process.

Mechanochemical approaches are well suited to generate products with small crystallite size and high defect concentration, while being environmentally friendly because the use of solvents and high sintering temperatures can often be avoided.[10] However, only a few mechanochemical processes to form $LiMn_2O_4$ without thermal annealing have been reported so far. A heat treatment usually cures the structure changes that were introduced during the milling process, therefore longtime stability of the prepared phases, for example under the conditions in a lithium ion battery are limited. In the known mechanochemical syntheses the effects of the milling process on crystal structure and microstructure have seldom been considered. A Rietveld refinement model to accommodate the X-ray diffraction peak shapes of mechanochemically processed $LiMn_2O_4$ has not been proposed yet. In the past, Kosova et al. have obtained $LiMn_2O_4$ by grinding a mixture of Li_2CO_3 and MnO_2 in an AGO-2 planetary ball mill.[11] Patterns with broad reflections were obtained, but no interpretation in terms of crystallite size or strain was reported in this study and the ideal cubic structure was assumed. Choi et al. have obtained $LiMn_2O_4$ by treating Li_2O and MnO_2 in a Spex 8000 shaker mill.[12] No lattice parameters were reported, but crystallite size and strain have been evaluated via a Williamson hall plot by single line fitting. A strong contribution to the reflection broadening by strain was proposed, suggesting a high degree of disorder in the structure. Crystallographic structure changes were not considered in this investigation. Disordered cation sites have also been indicated by ^7Li solid-state NMR of $LiMn_2O_4$ from a mechanochemical

[a] Saarland University,
Inorganic Solid-State Chemistry,
Campus C4 1, 4. OG, 66123 Saarbrücken, Germany
E-mail: guido.kickelbick@uni-saarland.de

Supporting information and ORCID(s) from the author(s) for this article are available on the WWW under https://doi.org/10.1002/ejic.201900946.

synthesis from LiOH or Li_2CO_3 with MnO_2.[13] A severe broadening of reflections occurs similarly by milling $LiMn_2O_4$ from a solid-state reaction.[14] The ideal cubic spinel structure was assumed, and the reflections were fitted independently to estimate the ratio of crystallite size and strain broadening. In a different work, a Rietveld refinement based on the cubic spinel structure was conducted.[15] Considerable misfits are present due to an anisotropic broadening of the reflections, which is hardly recognizable by single peak fitting. Strain and crystallite size of milled $LiMn_2O_4$ cannot be evaluated satisfactorily in a Rietveld refinement based on the ideal cubic spinel structure.

The idealized structure of stoichiometric $LiMn_2O_4$ is the cubic spinel structure with space group $Fd\bar{3}m$. The structure is formed by a cubic close packing of oxygen atoms on the 32*e* site. Li cations occupy 1/8 of the tetrahedral voids on the 8*a* site. Mn(III) and Mn(IV) cations occupy 1/2 of the octahedral voids on the 16*d* site.[3] The Jahn–Teller distortion of Mn(III) is compensated by the statistical distribution of Mn(III) and Mn(IV) cations. A structure representation is given in Figure 1.

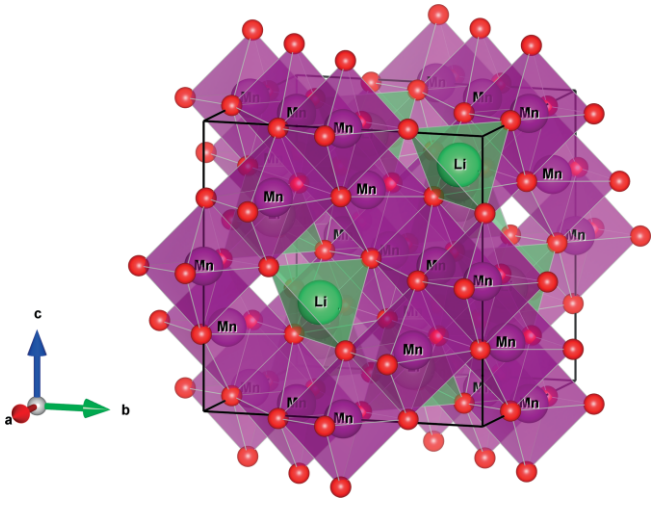

Figure 1. Idealized crystal structure of spinel $LiMn_2O_4$. Image generated with VESTA.[16]

Cubic spinel $LiMn_2O_4$ is the typical phase used in battery applications.[1,2,5] However, beside the cubic spinel, orthorhombic, and tetragonal structures are also known. Below 10 °C, a splitting of the spinel reflections is observed, indicating a lowering of the symmetry. A phase transition to an orthorhombic low temperature phase, with a cell volume nearly identical to the cubic structure, is encountered.[17] Neutron powder diffraction data have been refined with an orthorhombic structure based on a 3x3x1 super cell of cubic spinel, to describe the cation distribution more accurately.[18] The models of ideal cubic spinel at room temperature and the orthorhombic structure below 10 °C have also been confirmed by single-crystal X-ray diffraction.[19] A combined approach of Rietveld refinement and pair distribution function refinement for neutron diffraction data of $LiMn_2O_4$ reveals that the orthorhombic structure is already present at room temperature in the form of a short-range ordering.[20] Cooling of the sample induces the expected transformation to an orthorhombic state with a long-range ordering. The orthorhombic structure has also been stabilized applying pressures of 2 to 3 GPa at room temperature and up to 415 K.[21] The tetragonal structure of $LiMn_2O_4$ is either obtained by lithium intercalation (forming $Li_{1+x}Mn_2O_4$) or by oxygen deficiencies or a surplus of manganese.[22,23] In both cases, the concentration of Mn(III) is high enough for the Jahn–Teller effect of Mn(III) to induce a *c*/*a* splitting and subsequently a tetragonal symmetry.

No structure models have been proposed so far to properly describe the changes in the patterns of milled $LiMn_2O_4$ in a Rietveld refinement. The goal of our study is to evaluate the milling induced crystallographic structure changes and microstructure changes in $LiMn_2O_4$. To prevent a decomposition of $LiMn_2O_4$ in the milling process, phenylphosphonic acid is added as surface functionalization agent. By considering an orthorhombic symmetry and cation disorder, the peak shapes that are dominated by strain can be fitted with a multi-fraction model.[24,25] A broad distribution of different states, even with changes in the symmetry between orthorhombic, tetragonal and cubic, can be described in this way. Three different states in the samples are defined and the thermal stability of these states is evaluated via in situ high temperature PXRD measurements.

2. Results and Discussion

Milling of coarse-grained $LiMn_2O_4$ prepared in a high temperature solid-state reaction (ssr-LMO) should lead to a reduction of the crystallite size. However, a decomposition of the spinel phase can be observed at harsher milling conditions (Figure 2). New reflections, matching the pattern of Mn_2O_3 are formed. This is accompanied by an uneven and wave-like background indicating the formation of amorphous and unknown poorly crystalline phases. The decomposition is observed at a high milling speed (600 rpm) or prolonged milling times of more than 6 h at medium milling speed (400 rpm).

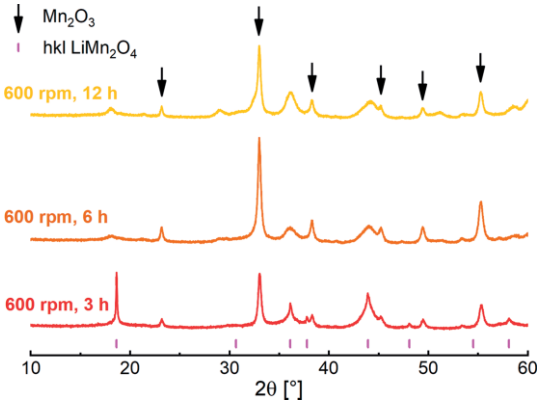

Figure 2. Powder X-ray diffraction patterns of $LiMn_2O_4$ milled for 3, 6 and 12 h at 600 rpm. Arrows indicate reflections of Mn_2O_3. The lines indicate the hkls of spinel $LiMn_2O_4$.

We investigated whether the decomposition can be avoided if a surface capping agent is added, such as phenylphosphonic acid (PPA). In previous studies we were able to show that in situ surface-functionalization during milling has beneficial effects on the phase stabilization.[26–28] The addition of PPA in the mill-

ing process retains the original reflection pattern even at higher milling speeds and longer milling times, without the formation of clearly visible amounts of Mn_2O_3 or an amorphous phase. Therefore, only the results obtained by milling ssr-LMO with PPA (consecutively referred to as ball milled LMO or bm-LMO) are discussed in the following sections. Since PPA forms covalent bonds with the surface of $LiMn_2O_4$ in the milling process it is assumed that PPA acts as not only a dispersing agent, but also that the in-situ surface functionalization itself plays an integral role in retaining the spinel structure. The formation of a covalent bonds between a phosphonic acid and a metal oxide can be detected by infrared (IR) spectroscopy and has already been established in literature.[26–28] To form a stabilizing surface functionalization, the amount of PPA should be as high as possible. A homogeneous powder was formed up to 10 wt.-% of PPA. Higher amounts lead to cementing of the powder in the grinding jar. The IR spectra of the milling products of $LiMn_2O_4$ with 10 wt.-% PPA at 400 rpm are shown in Figure 3. The IR spectra of 200 and 600 rpm milled $LiMn_2O_4$-PPA mixture are presented in the supporting information (Figure SI 1 and Figure SI 2) and exhibit comparable features.

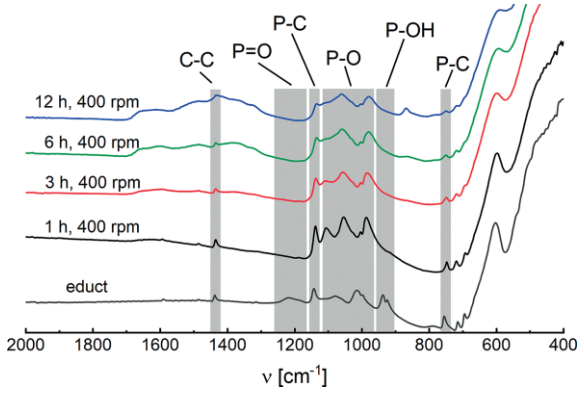

Figure 3. FT-IR spectra of $LiMn_2O_4$ with PPA before (educt) and after milling at 400 rpm for different milling times.

The assignment of the IR bands was carried out according to the published data of Guerrero et al. and Botelho do Rego et al.[29,30] The characteristic bands of the phosphorus oxygen vibrations are found in the range between 900 and 1200 cm^{-1} and reveal whether the phosphonic acid is covalently attached to the surface or not. Generally, surface functionalization of metal oxides takes place due to the condensation reaction of P-OH and P=O groups of the phosphonic acid group with free *M*=O and *M*-OH groups on the metal oxide surface.[29] After 1 h milling time at 400 rpm a small peak of the P-OH vibration located in the range of 740 to 760 cm^{-1} can still be detected, indicating no full condensation of the phosphonates with the surface. After 3 h the signal has completely vanished. Additionally, the distinct signal of the P=O double bond, visible at 1160 to 1260 cm^{-1} in the unmilled starting material mixture, disappears completely after 1 h of milling. Since no further changes between 900 and 1200 cm^{-1} occur applying longer milling times, the surface functionalization is completed after approximately 3 h at a milling speed of 400 rpm. At 200 rpm the functionalization is completed only after 12 h milling time. At 600 rpm the functionalization is already completed after 1 h milling time. The surface functionalization is therefore dependent on both, milling time and milling speed. In contrast to the P–O vibrations, the C–C and P–C vibrations are less affected. Prolonged milling leads to a slight decrease in intensity of the C–C and P–C vibrations, indicating a partial decomposition of the phenyl groups. The emerging broad signal between 1300 and 1700 cm^{-1} matches the typical signal observed for metal carbonates.[31] Since no crystalline carbonate species like Li_2CO_3 or $MnCO_3$ were visible in the PXRD patterns, it is assumed that only small amounts of a carbonate species are formed on the surface of the product. Since the appearance of the carbonate signal coincides with the decrease of the phenyl group signals, it is possible that the carbonate formation is the product of the phenyl group decomposition. The uptake of carbon dioxide from surrounding air cannot be excluded, however.

Scanning electron microscopy (SEM) images of ssr-LMO milled with PPA at 200, 400 and 600 rpm for 12 h reveal the formation of small particles (Figure 4). The particle size of ssr-LMO is in the range of several microns. The milled products on the other hand reveal particles much smaller than 1 µm, which form larger agglomerates. The surface area of the milled products may still be assumed to be much larger than the surface area of ssr-LMO.

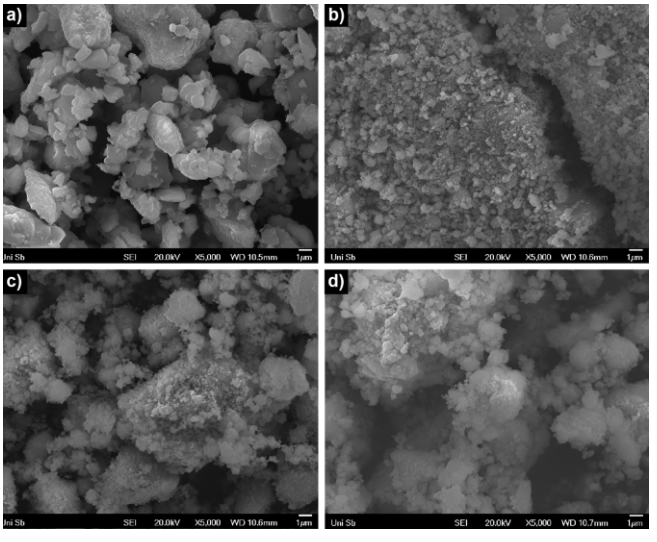

Figure 4. SEM images of $LiMn_2O_4$ after (a) solid-state reaction, (b) milling with PPA at 200 rpm for 12 h, (c) milling with PPA at 400 rpm for 12 h, and (d) milling with PPA at 600 rpm for 12 h. Factor of magnification: 5000.

After milling ssr-LMO with PPA in a high energy ball mill, three product states were differentiated via PXRD (Figure 5). Milling at a low milling speed of 200 rpm for up to 6 h produces a coarse-grained fraction with sharp reflections on top of broad reflections corresponding to a fine-grained fraction. The low milling speed may lead to inhomogeneities in the milling process. It is assumed that there are not enough ball impact events in the given milling time to affect every powder particle. A longer milling time of 12 h compensates this and leads to a product, which does not reveal sharp reflections anymore. This marks the first state of the milling products, referred to as **state A**. A very dominant strain effect leads to an anisotropic reflec-

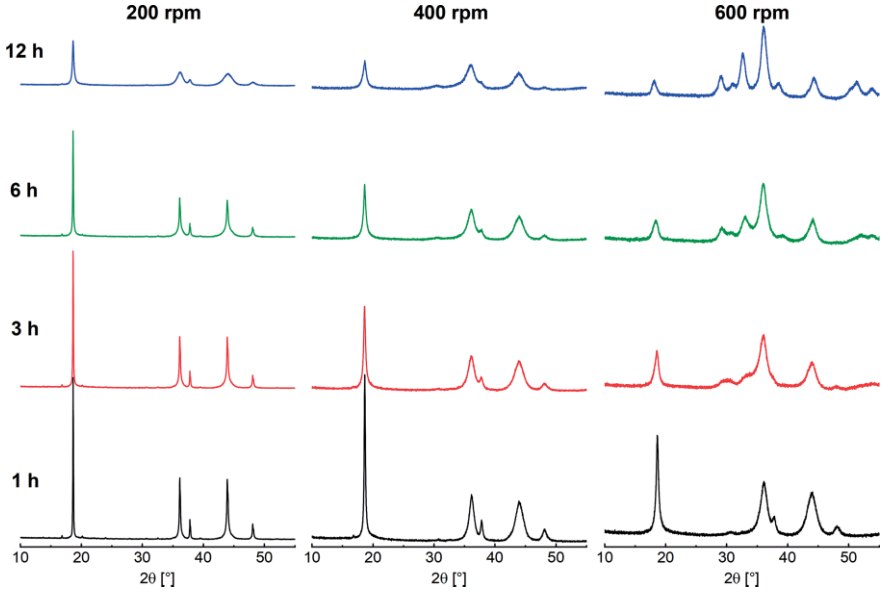

Figure 5. Overview of the powder patterns of $LiMn_2O_4$ with PPA after milling at 200, 400 and 600 rpm for 1, 3, 6, and 12 h, respectively.

tion broadening, like it has already been mentioned by Kang et al. and Kamarulzaman et al.[14,15] This state extends to the products obtained from a milling speed of 400 rpm up to a milling time of 3 h. Further milling initiates the second observed state, in which the reflection intensities start to change, indicating an additional variation of the atomic positions. This state is referred to as **state B**. The third state, referred to as **state C**, is characterized by a clear change in symmetry to a tetragonal state with an elongated *c* axis. This transformation is already indicated after milling at 400 rpm for 12 h and becomes very prominent at a milling speed of 600 rpm, visible by the formation of new reflections around 30° 2θ. A nearly complete transformation is observed after prolonged milling at 600 rpm.

2.1. Product States after Milling

2.1.1. State A: Anisotropic Reflection Broadening

The typical phase transformation of ssr-LMO to the orthorhombic low temperature phase is not present in bm-LMO. A comparison of low temperature in situ XRD patterns of ssr-LMO and bm-LMO is shown in Figure 6. Upon cooling, the splitting of the (311) reflection of ssr-LMO can be observed. The PXRD patterns of bm-LMO, in comparison, show no changes. The absence of a phase transformation is also confirmed by DSC measurements (Figure 6). In the DSC curve of ssr-LMO the expected signal corresponding to the phase transformation to the orthorhombic phase is visible at 7°C. The DSC curve of bm-LMO however reveals no signals.

Since in situ low temperature XRD and DSC measurements have demonstrated the absence of a phase transformation, a Rietveld refinement with an orthorhombic structure may be more adequate. To verify this, different structure models were investigated and compared (Figure 7). The fit quality was based on a comparison of the *weighted profile R-factors* (R_{wp}) and, as an additional criterion, the *goodness of fit* values (*GOF*). The *GOF* is calculated from the ratio of the *weighted profile R-factor* (R_{wp}) and the *expected R-factor* (R_{exp}).[32]

The first refinement was conducted based on the ideal spinel structure and is shown in Figure 7a. As expected, a severe misfit

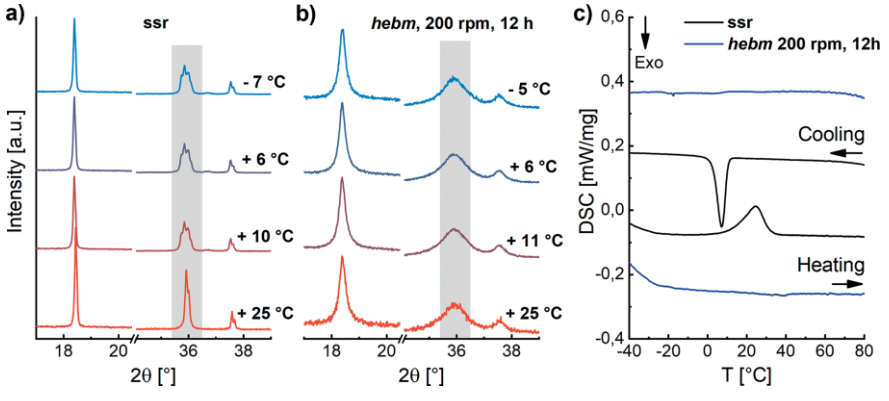

Figure 6. Occurrence and absence of the low temperature phase transition in un-milled (ssr) and milled (hebm, 200 rpm, 12 h) $LiMn_2O_4$ respectively, as seen via low temperature in situ XRD and DSC measurements. (a) In situ XRD of un-milled (ssr) $LiMn_2O_4$, (b) in situ XRD of milled $LiMn_2O_4$, and (c) DSC curves of un-milled (black) and milled (blue) $LiMn_2O_4$.

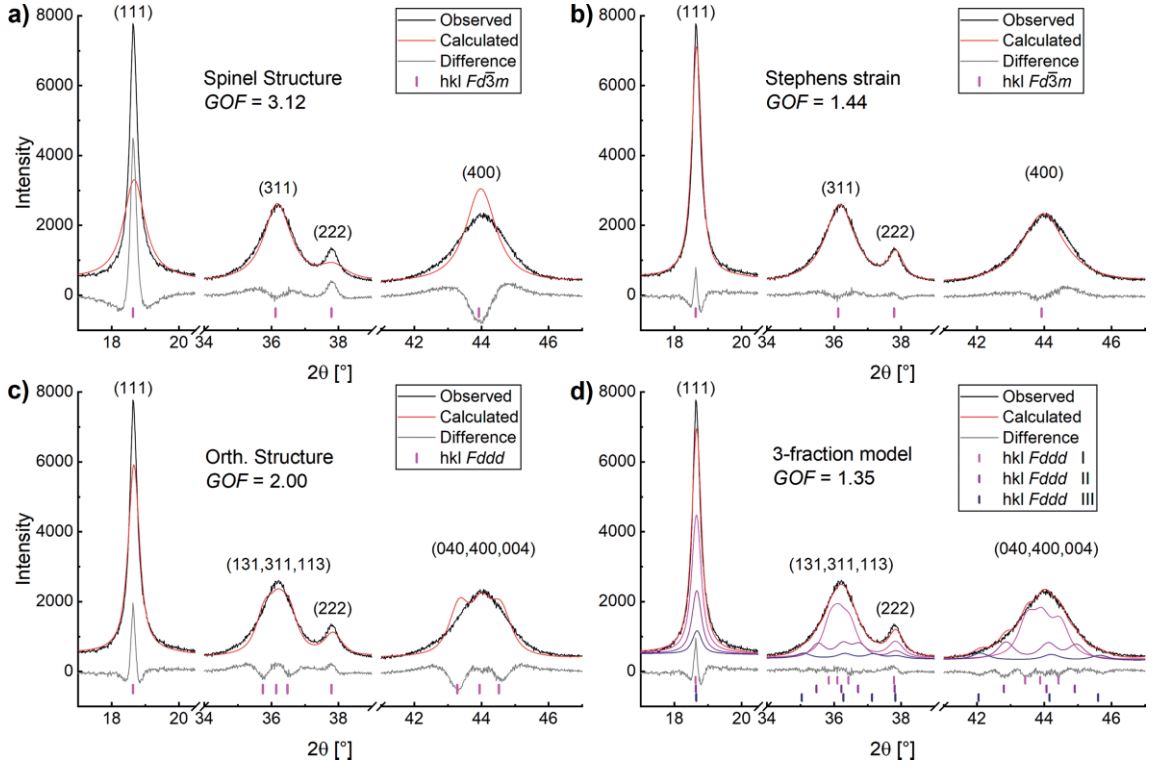

Figure 7. Rietveld refinements of milled $LiMn_2O_4$ (200 rpm, 12 h) with (a) spinel structure, (b) spinel structure with Stephens strain model (as implemented in TOPAS 5), (c) orthorhombic structure, and (d) three-fraction model with orthorhombic structure.

is observed especially in the case of the (111) reflection. The misfit of the refinement is reflected by a high R_{wp} of 12.65 % and GOF of 3.12. The anisotropic broadening of the reflections can be better described by use of the Stephens strain model with cubic symmetry, as implemented in TOPAS 5.[33] This leads to a highly improved description of the line-shape, with an R_{wp} of 5.86 % and a GOF of 1.44 (Figure 7b). The Stephens model is based on the variation of lattice parameters, but it is difficult to derive this variation directly. To simulate this distribution more easily, a refinement of several independent lattice parameters is necessary. Therefore, the refinement was based on a pseudo cubic spinel structure with three independent lattice parameters, which is achieved by changing the space group of the spinel structure from $Fd\bar{3}m$ to *Fddd*. Since the space group *Fddd* of the orthorhombic low temperature structure is a subgroup of $I4_1/amd$, which again is a subgroup of the space group $Fd\bar{3}m$, the atomic positions and initial lattice parameters were kept the same as in the spinel structure. This simple orthorhombic model now allows to simultaneously refine pseudo cubic, pseudo tetragonal and orthorhombic cells, which are directly comparable to each other.

It has already been shown by Hayakawa et al. that a refinement of the orthorhombic low temperature phase of $LiMn_2O_4$ with a cell of similar volume as the spinel structure, yields a reasonable fit of X-ray diffraction data.[17] Additionally, the simple orthorhombic structure model leads to a lower number of parameters compared to the established *Fddd* 3x3x1 superstructure, and therefore to a more stable refinement. This observation is confirmed by refinements of our in situ low temperature measurements of ssr-LMO. A refinement with the full orthorhombic 3x3x1 superstructure model yields an R_{wp} of 7.23 % and a *GOF* of 1.29. A refinement with the simple orthorhombic model yields an R_{wp} of 8.45 % and a *GOF* of 1.50. The slight loss in fit quality is acceptable, since a faster and much more stable refinement is achieved.

Figure 7c shows a refinement based on the simple orthorhombic structure model. An improved fit compared to the ideal cubic spinel structure model in Figure 7a is achieved, however there are still significant misfits expressed by an R_{wp} of 8.11 % and a *GOF* of 2.00. Since the tailing of the (311) and (400) reflection group is still not accurately described a more nuanced variation of the lattice parameters is necessary. A multi-fraction model to describe the fluctuation of lattice parameters has already been described for a series of chlorovanadato-apatites and sodium vanadates.[24,25] To introduce additional increments, a refinement with three fractions of the proposed simple orthorhombic structure model is conducted. The nine generated lattice parameters are refined independently while the microstructural parameters (crystallite size and strain broadening) and atomic positions are constrained to be the same value for all fractions. This approach prevents an overparameterization of the refinement, while allowing to directly visualize the distribution of the lattice parameters. Additionally, this model allows to fit asymmetric reflections, since the median lattice parameters of the fractions are independent of each other. The result of the refinement is shown in Figure 7d and yields the best fit of the four refinement methods, with an R_{wp} of 5.49 % and a *GOF* of 1.35. The quality of the fit may be even further increased by applying an eleven-fraction model with equidistant fractions, simulating a probability distribution of

different lattice parameter sets.[25] Using this approach an R_{wp} of 5.14 %, a *GOF* of 1.27, and a much smoother peak profile can be obtained. However, this model does not allow the refinement of changes in the symmetry and the refinement speed is much lower. Therefore, we applied the three-fraction model with the simple orthorhombic structure and independent lattice parameters in our further studies.

The distribution of the lattice parameters obtained from the three-fraction model with the simple orthorhombic structure is shown in Figure 8. The lattice parameters range in total from 7.950(2) Å to 8.590(2) Å, with the weight of these parameters being 10 % (Fraction III). The weighted mean value is found to be 8.242 Å, which is quite close to the lattice parameter of ideal cubic spinel $LiMn_2O_4$ of 8.245 Å applied as starting material in the milling process. The refined crystallite size <L> is 35(1) nm.

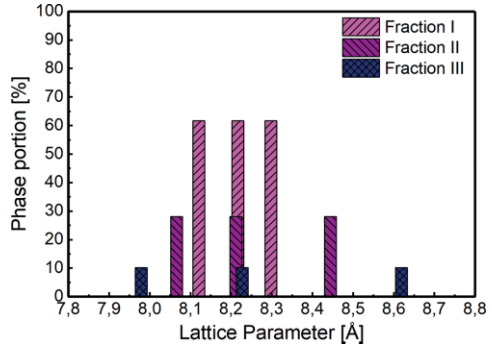

Figure 8. Distribution of lattice parameter from Rietveld refinement with three fractions of orthorhombic $LiMn_2O_4$ with space group *Fddd*.

2.1.2. State B: Intensity Variation

As already mentioned, prolonged milling at 400 rpm induces an additional change of the relative reflection intensities. This is most probably caused by a change in the cation distribution. A cation disorder in mechanochemically synthesized $LiMn_2O_4$ has already been proposed by Kosova et al. by ^{7}Li solid-state NMR measurements.[13] To refine the cation distribution, the site occupation factors (*sof*) of the lithium and manganese positions were constrained to yield a stoichiometric composition of the sample, while the oxygen *sof* was kept constant. One additional manganese atom was defined at the lithium 8*a* site and one additional lithium atom at the manganese 16*d* site. To provide more clarity, the sites of the cations filling the tetrahedral or octahedral voids of the (distorted) cubic close packed oxygen layers are named Li_tet and Mn_oct in the following discussion. One *sof* was refined as a free parameter and the *sofs* of the remaining three atoms are constrained to ensure a constant electron density. The dependence of the *sofs* of the lithium and manganese sites is summarized in Table 1.

Table 1. Constraint to refine a combined sof of the lithium and manganese sites.

Site	*WP*	Atom	*sof*
Li_tet	8*a*	Li^+	x
		$Mn^{3.5+}$	= 1 − *x*
Mn_oct	16*d*	$Mn^{3.5+}$	= 1/2·(1 + *x*)
		Li^+	= 1/2·(1 − *x*)

The change of the relative intensities is very dominant in the sample milled at 400 rpm for 12 h (bm-LMO-400–12). The

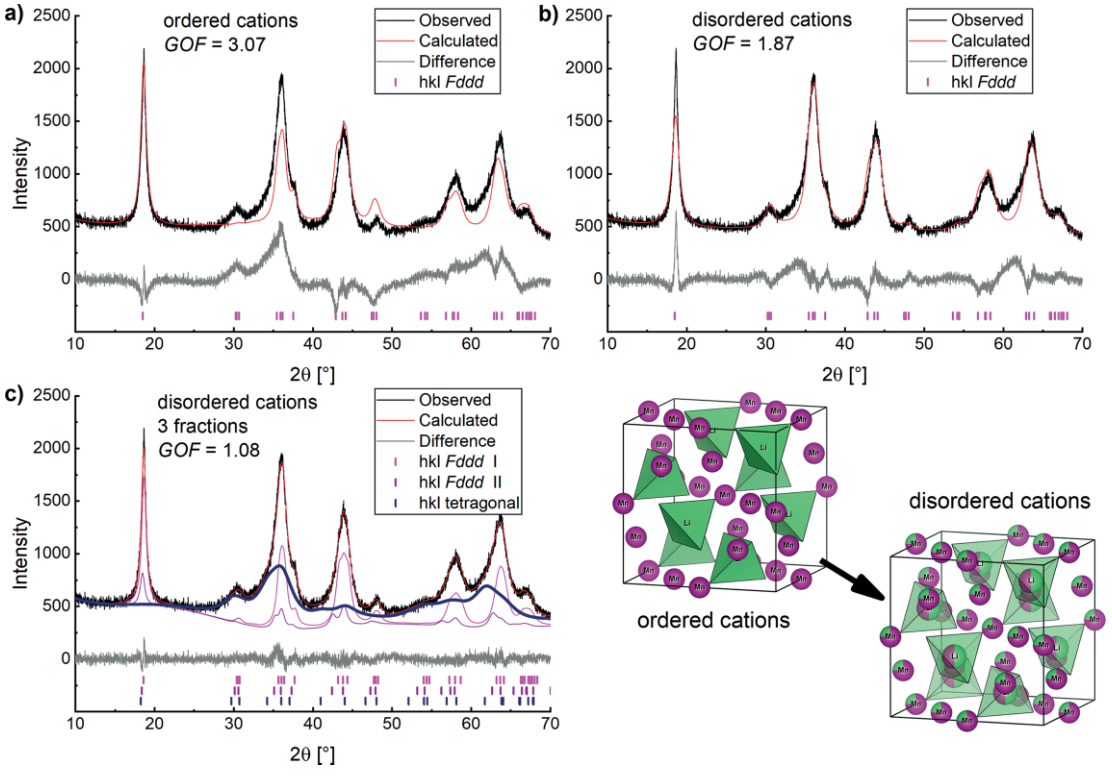

Figure 9. Rietveld refinements of bm-LMO-400–12 (milled $LiMn_2O_4$, 400 rpm, 12 h) with (a) single fraction orthorhombic structure, (b) disordered cation distribution, and (c) three-fraction model with disordered cation distribution. The structure illustration shows the cation disordering. Structure representations generated with VESTA.[16]

Table 2. Structure model to refine two constrained orthorhombic (I+II) and a tetragonal fraction (III), both with disordered cation distributions.

Frac.	Site	*WP*	*x*	*y*	*z*	Atom	sof	B_{iso}
	Li_tet1	8*a*	1/8	1/8	1/8	Li^{+}	0.87(1)	1.5(1)
						$Mn^{3.5+}$	0.13(1)	1.5(1)
I+II	Mn_oct1	16*d*	1/2	1/2	1/2	$Mn^{3.5+}$	0.93(1)	1.5(1)
						Li^{+}	0.07(1)	1.5(1)
	O1	32*e*	0.2642(3)	0.2642(3)	0.2642(3)	O^{2-}	1	1.3(1)
	Li_tet2	8*a*	1/8	1/8	1/8	Li^{+}	0.25(1)	1.5(1)
						$Mn^{3.5+}$	0.75(1)	1.5(1)
III	Mn_oct2	16*d*	1/2	1/2	1/2	$Mn^{3.5+}$	0.62(1)	1.5(1)
						Li^{+}	0.38(1)	1.5(1)
	O2	32*e*	0.241(1)	0.241(1)	0.241(1)	O^{2-}	1	1.3(1)

differences in the refinements with and without a cation disorder is presented in Figure 9. A refinement with a single fraction of the simple orthorhombic model with an ideal spinel cation distribution ($x = 0$) is shown in Figure 9a. While the intensity of the first reflection is calculated accurately, the intensities of the following reflections are severely mismatched. A refinement with a single fraction of the simple orthorhombic model with a cation disorder within the scope of the proposed constraint is shown in in Figure 9b. The relative intensities of the reflections are described more accurately by this model. In Figure 9c a refinement with the three-fraction model is shown. In contrast to the milling products at 400 rpm with up to 6 h milling time, only two of the fractions show lattice parameters that are still close to the cubic spinel after 12 h milling time. The third fraction exhibits two lattice parameters being nearly identical ($a = b = 8.219(3)$ Å) and a third being much longer ($c = 8.796(8)$ Å). It may be assumed that a new phase with tetragonal symmetry is forming. To accommodate this, the microstructure and cation distribution of fraction III was refined independently from fraction I and II. A weight portion of 58 % is refined for the pseudo tetragonal fraction III, while fraction I and II account for 33 % and 9 %, respectively. The refined crystallite size <L> of fraction I and II is 11.2(2) nm. To highlight the portion of the pseudo tetragonal fraction III, the line was plotted thicker. Since the reflections are extremely broad it may be assumed that very small domains with tetragonal symmetry are formed. The refined crystallite size <L> of fraction III is 3.3(1) nm.

The resulting cation distribution of the refinement with the revised three-fraction model is shown in Table 2. The constrained fractions I and II are still close to the cation distribution of the normal spinel and exhibit a disorder of more than 25 %. The now independent and tetragonal fraction III on the other hand shows a cation distribution more similar to an inverse spinel structure, with the 8*a* site being occupied mostly by manganese.

2.1.3. State C: Phase Transformation

After milling $LiMn_2O_4$ with PPA at 600 rpm for 12 h (bm-LMO-600–12) the proposed pseudo tetragonal state has formed with sharper reflections (Figure 10). A phase portion of 87 % is refined. The crystallite size is determined to be 7.1(2) nm. The remains of fraction I and II accommodate the shape of residual reflections intensities that may still arise from the presence of small portions of $LiMn_2O_4$ with orthorhombic symmetry or pseudo tetragonal symmetry with a less distinct splitting. The pseudo tetragonal main phase exhibits a reflection broadening mostly dominated by the crystallite size. The strain contribution is quite low and no anisotropic broadening of the reflections was detected. The complete refinement parameters of the tetragonal phase are summarized in the supporting information in Table SI 1.

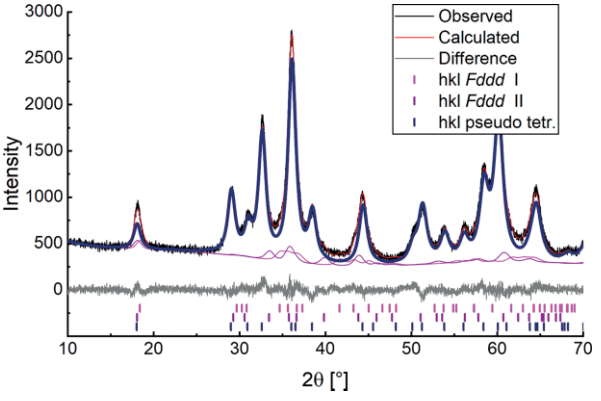

Figure 10. Rietveld refinement of bm-LMO-600–12 (milled $LiMn_2O_4$, 600 rpm, 12 h) with a three-fraction model with disordered cation distribution.

The reflection pattern of the formed phase is very similar to that of tetragonal Hausmannite Mn_3O_4 with space group $I4_1/amd$. To exclude the possibility that pure Mn_3O_4 has formed, the lattice parameters, lattice ratios, and cell volumes of both phases can be compared. The Mn_3O_4 structure is a tetragonal distorted spinel structure and directly related to the cubic spinel structure via the symmetry reduction from the space group $Fd\bar{3}m$ to $I4_1/amd$. The spinel *aristo* structure (and the proposed simple orthorhombic *Fddd* structure model) can be represented as $\sqrt{2}x\sqrt{2}x1$ superstructure of the tetragonal $I4_1/amd$ structure. The lattice parameters are summarized in Table 3.

Table 3. Lattice parameters of bm-LMO-600–12 compared to the lattice parameters of a Mn_3O_4 reference sample from a solid-state reaction (ssr).

Phase	*a* [Å]	*c* [Å]	*c*/*a*	*V* [Å^3]
bm-LMO-600–12	5.7777(5)·√2	9.3652(8)	1.621	312.6(1)
ssr-Mn_3O_4	5.76237(2)	9.47011(3)	1.643	314.45(1)

It can be seen that sample bm-LMO-600–12 exhibits a lower cell volume than Mn_3O_4. The *a* lattice parameter of the milled product is longer, while the *c* axis is much shorter. Since the tetragonal splitting of Mn_3O_4 is caused by the Jahn-Teller distortion of the Mn(III) cations, a less pronounced splitting suggests

a lower Mn(III) content in the bm-LMO-600–12 sample. It is assumed that this difference is caused by the lithium content. A refinement of the constrained *sof* indicates that 30 % of lithium is located in the tetrahedral voids and 70 % in the octahedral voids. This observation is again an indication for a lower Mn(III) content, since Mn(III) is located in the octahedral voids and therefore substituted by lithium. A tetrahedral coordination of Mn(III) is very unlikely. This is however based on the assumption of an unchanged $LiMn_2O_4$ stoichiometry. The lithium content may be lower than 1 but is most certainly higher than 0 based on the refined lattice parameters and *sof*. A co-refinement of X-ray and neutron powder data, which will be published elsewhere, yields a lithium content of approximately 0.6 (i.e. $Li_{0.6}Mn_{2.4}O_4$).

2.2. Thermal Stability

The thermal stability of the three proposed product states is evaluated via in situ high temperature PXRD experiments. The products obtained from milling at 200, 400, and 600 rpm for 12 h were selected as representative samples. The sample milled at 200 rpm (bm-LMO-200–12) is dominated by the anisotropic reflection broadening. The sample milled at 400 rpm (bm-LMO-400–12) is additionally affected by intensity changes, correlated to the cation disorder. The sample milled at 600 rpm (bm-LMO-600–12) represents the state of the transformation to the tetragonal phase. A heat map of the in situ XRD data of the bm-LMO-200–12 sample is shown in Figure 11. The heat maps of the samples bm-LMO-400–12 and bm-LMO-600–12 are shown in the supporting information Figure SI 3 and Figure SI 4, respectively.

The heat map of bm-LMO-200–12 reveals only gradual changes of the pattern up to a temperature of 300 °C. From 300 °C new reflections start to emerge up to about 450 °C, where the former main reflections have nearly vanished. A change back to the initial reflection pattern can be observed with increasing temperature. At 600 °C a pattern with sharper reflections than the milled product is obtained. Additional reflections are visible, indicating the formation of a side phase. The samples milled at 400 and 600 rpm behave similarly, though the change of the initial pattern and the formation of new reflections is observed at lower temperature with increasing milling speed. Rietveld refinement with the proposed three-fraction model with the simple orthorhombic structure was applied to all recorded patterns to follow the thermal induced changes in the patterns. This allows a simultaneous refinement of anisotropic reflection broadening, cation distribution and formation of phases with pseudo cubic, pseudo tetragonal and orthorhombic symmetry. The collected results, in the form of phase portions and lattice parameters for the three fractions, are summarized in Figure 12, Figure 13, and Figure 14 for the products milled at 200, 400 and 600 rpm, respectively.

For sample bm-LMO-200–12, no significant changes of the lattice parameters or the phase portions of the three fractions are visible up to a temperature of 200 °C. Only an expectable thermal expansion of the lattice can be interpreted. The crystallite <L> remains around 33 nm in this temperature range. At 250 °C, the crystallite size increases to 51(1) nm. Additionally, two nearly identical lattice parameters are refined for fraction III. To adjust the refinement, these were constrained to be equal and the microstructure of fraction III was refined independently from fraction I and II. Since the third lattice parameters be-

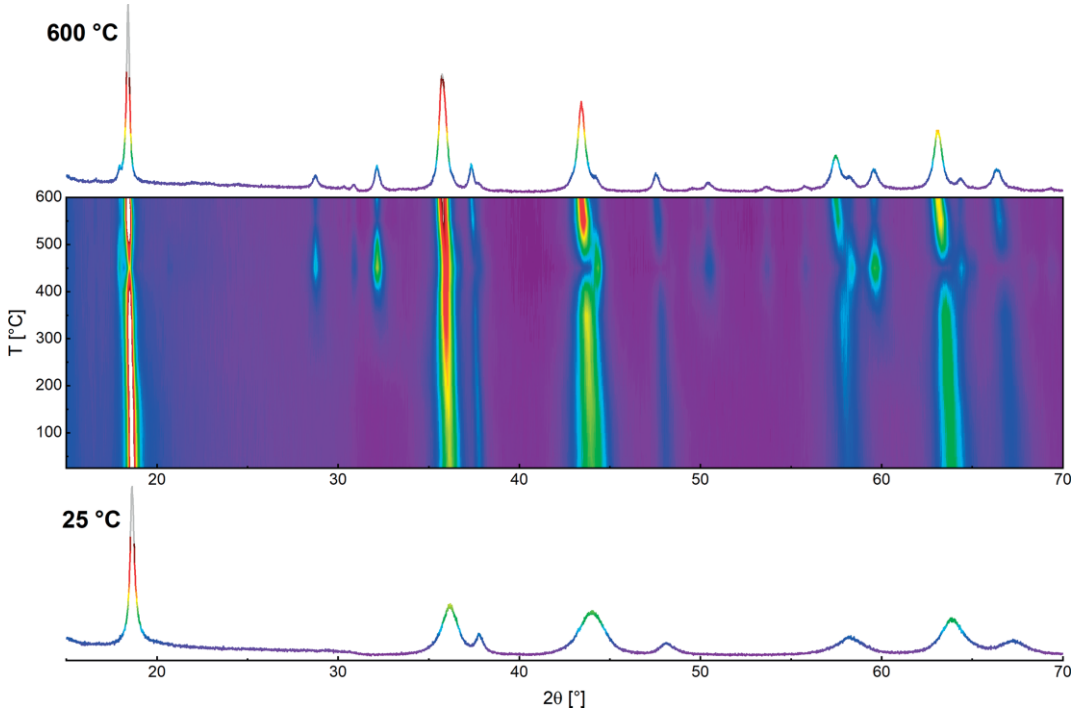

Figure 11. In situ XRD measurements of $LiMn_2O_4$ after milling with PPA at 200 rpm for 12 h. The lower pattern was recorded before heating and the upper pattern was recorded at 600 °C.

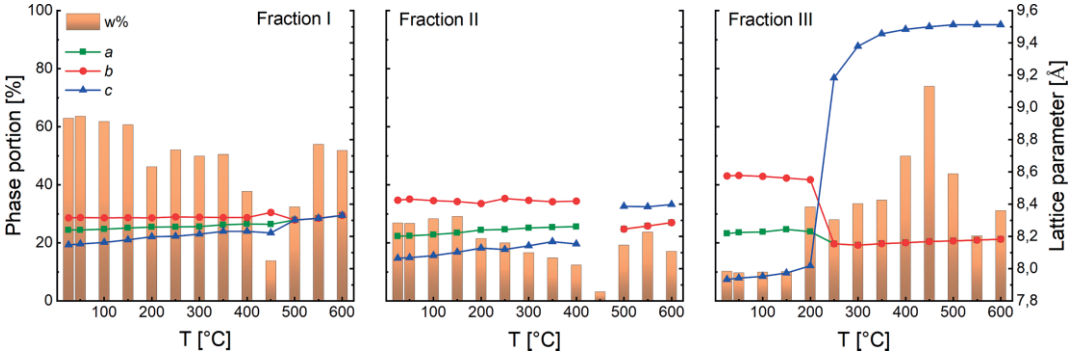

Figure 12. Phase portions (orange bars) and lattice parameters (green, red and blue lines) from Rietveld refinement of the in situ XRD measurements with the three-fraction model. $LiMn_2O_4$ milled at **200 rpm** for 12 h.

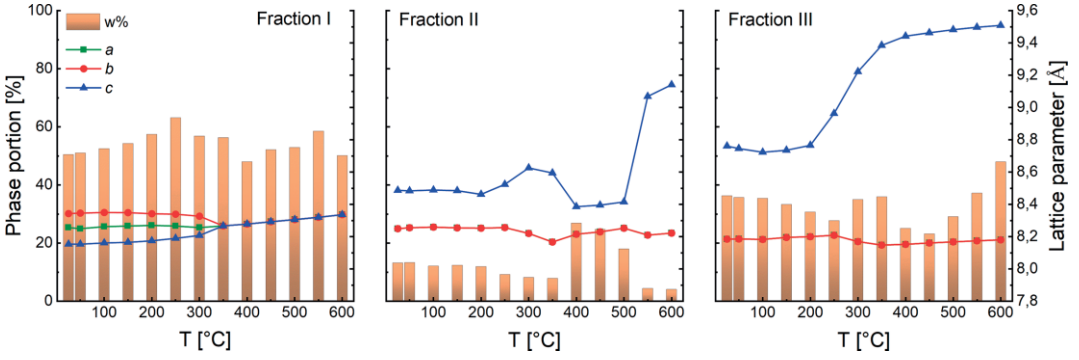

Figure 13. Phase portions (orange bars) and lattice parameters (green, red and blue lines) from Rietveld refinement of the in situ XRD measurements with the three-fraction model. $LiMn_2O_4$ milled at **400 rpm** for 12 h.

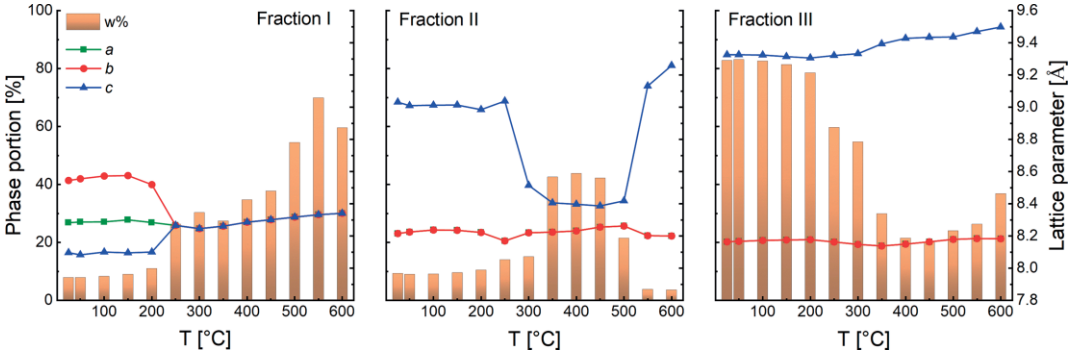

Figure 14. Phase portions (orange bars) and lattice parameters (green, red and blue lines) from Rietveld refinement of the in situ XRD measurements with the three-fraction model. $LiMn_2O_4$ milled at **600 rpm** for 12 h.

comes much longer, it may be assumed that a tetragonal phase appears that is similar to the phase formed after milling at 600 rpm for 12 h. The crystallite size of the tetragonal fraction III is refined to 2.6(2) nm. The phase portion and crystallite size of the tetragonal phase increase rapidly with increasing temperature until a maximum is reached at 450 °C. A portion of 73 % and a crystallite size of 20(1) nm is refined. In contrast, the crystallite size of fraction I and II decreases slightly to 41(1) nm. The phase portion of fraction II is very low at this point. Therefore, a reliable refinement of the lattice parameters was not possible. The orthorhombic splitting of the lattice parameters of fraction I becomes larger, probably to compensate the low amount of fraction II. Additionally, new reflections corresponding to the lithium rich phase Li_2MnO_3 can be refined with a phase portion of about 10 %. This indicates a segregation of the initially single-phase product. The formation of Li_2MnO_3 has also been observed by in situ high temperature XRD of cubic spinel $LiMn_2O_4$ to temperatures above 900 °C.[34] To exclude the formation of pure tetragonal Mn_3O_4 as fraction III, cell parameters of a Mn_3O_4 reference sample were refined over the complete temperature range of the in situ XRD measurements. Pure Mn_3O_4 reveals a volume constantly about 2 $Å^3$ larger than that of fraction III. This indicates that the formed tetragonal phase at least partly contains lithium. However, the lithium content is probably lower than in $LiMn_2O_4$. The overall cell volume of fraction III is much larger than of fraction I and II, which may be

based on a higher Mn(III) content. Further heating to 500 °C induces a decrease of the phase portion of fraction III and an increase of fraction I and II. It is assumed that the probable lithium poor fraction III reacts with Li_2MnO_3 as the phase portion of the latter decreases significantly and vanishes completely in the next heating step. Since the splitting of the lattice parameters of fraction I decreases significantly, the three parameters were constrained to refine a cubic state. Fraction II now too exhibits two nearly identical lattice parameters and presumably compensates the still slightly anisotropic broadened reflections of the spinel pattern. The last heating steps up to 600 °C reveal no changes of lattice parameters except for the thermal expansion. The final crystallite sizes are 78(1) nm for fraction I and II and 30(1) nm for fraction III.

The changes in phase composition of the sample bm-LMO-400–12 (Figure 13) show a different behavior than sample bm-LMO-200–12. For sample bm-LMO-400–12 the microstructural parameters of fraction I and II are constrained, while fraction III is refined independently from the start. Additionally, fraction II and III are refined with tetragonal symmetry over the complete temperature range (lattice parameter *a* and *b* constrained).

The crystallite size of fraction I and II remains around 10 nm over the complete temperature range up to 600 °C. A final crystallite size of 13(1) nm is refined. The crystallite size of fraction III is 3.3(2) nm and increases to 27(1) nm at 600 °C. The transformation to cubic $LiMn_2O_4$ is found to occur at 350 °C. As soon as fraction I is refined with a cubic constraint of the lattice parameters, the tetragonal splitting of fraction II is decreased significantly in both samples. This is comparable to sample bm-LMO-200–12, since fraction II compensates the still slightly anisotropic reflection broadening of the cubic reflection pattern. Additionally, the phase portion of fraction II increases significantly in this way. Contrary to sample bm-LMO-200–12, no reflections of the lithium rich phase Li_2MnO_3 are observed for sample bm-LMO-400–12. Sample bm-LMO-600–12 (Figure 14) behaves very similar to sample bm-LMO-400–12. The same refinement constraints as described for sample bm-LMO-400–12 have been applied.

The crystallite size of fraction I+II and III is 7 nm in the beginning and increases to 18 and 20 nm respectively at 600 °C. The transformation to cubic $LiMn_2O_4$ is found to occur at an even lower temperature of 250 °C for sample bm-LMO-600–12. Overall, at 600 °C, all samples from 200 to 400 and 600 rpm milling speed show a consistent composition. The phase portion of the pseudo tetragonal fraction III is between 35 and 40 % and the phase portion of fraction II is very low. The lattice parameters of the pseudo tetragonal fraction III and the pseudo cubic fraction I is similar for each sample.

3. Conclusion

Phenylphosphonic acid functionalized nanocrystalline $LiMn_2O_4$ has been produced by dry milling of coarse-grained $LiMn_2O_4$ from a solid-state reaction with the respective phosphonic acid. The X-ray diffraction (XRD) patterns of the products are dominated by anisotropic reflection broadening, intensity changes, and formation of new reflections. A concise and versatile Rietveld refinement model to accommodate the XRD peak shapes has been proposed. The model is able to simultaneously describe the features of the patterns that are caused by a distribution of lattice parameters, cation disorder and formation of phases with orthorhombic, tetragonal and cubic symmetry. The thermal induced changes of the XRD patterns can also be described with this model.

4. Experimental Section

4.1. Materials

Li_2CO_3 (Merck, Darmstadt, Germany, 99 %), $MnCO_3$ (Alfa Aesar GmbH, Karlsruhe, Germany, 99.9 %), Mn_2O_3 (ChemPur, Karlsruhe, Germany, 99.9 %), phenylphosphonic acid (Sigma-Aldrich Chemie GmbH, Steinheim, Germany, 98 %), 2-propanol (Biesterfeld Spezialchemie, Hamburg, Germany, 97 %) and *n*-pentane (Sigma Aldrich, Steinheim, Germany, 99 %) were used as received. All precursor solids have been characterized by PXRD before use.

4.2. Sample Preparation

Spinel $LiMn_2O_4$ was synthesized via standard solid-state reaction from Li_2CO_3 and Mn_2O_3.[4] Stoichiometric amounts of the starting materials were homogenized by wet milling with *n*-pentane in an agate jar (volume of 50 mL) with 10 milling balls (diameter of 10 mm) of the same material. The powder mixture was milled at 400 rpm for 30 min. The mixture was dried in air and heated to 800 °C for 8 h in a platinum crucible. Mn_3O_4 reference material with the Hausmannite structure was synthesized by heating $MnCO_3$ in a platinum crucible to 1100 °C in air.[35] To prevent the formation of Mn_2O_3 the sample was quenched by removing the crucible from the hot furnace.

High energy ball milling was conducted with a planetary ball mill, type PM100 (Retsch, Germany). A grinding jar (volume of 50 mL) made of yttrium stabilized zirconia and 200 milling balls (diameter of 5 mm) of the same material were used. Approximately 3 g of starting powder were used, corresponding to a ball to powder weight ratio of 27:1. In-situ surface functionalization was achieved by adding 10 wt.-% phenylphosphonic acid. In the case of pure $LiMn_2O_4$, 200 µL of 2-propanol were added as dispersing agent to prevent cementing of the powder. The rotational speed of the mill was set to 200, 400 or 600 rpm.

4.3. Characterization

Powder X-ray diffraction (PXRD) patterns were recorded on a Bruker D8 Advance diffractometer (Bruker, Karlsruhe, Germany) in θ-θ-geometry (goniometer radius 280 mm) with Cu-K_α radiation (λ = 154.0596 pm, 40 kV, 40 mA). A 12 µm Ni foil was used to reduce K_β radiation. A variable divergence slit was mounted at the primary beam side (irradiated sample area of 10 × 7 mm). A LYNXEYE 1D detector was used at the secondary beam side. The background caused by white radiation and sample fluorescence was reduced by limiting the energy range of the detection.

Standard measurements were carried out in a 2θ range of 7 to 120° with a step size of 0.013° and a total scan time of 2 h. In situ low temperature XRD was realized by using a self-constructed sample holder with thermoelectric cooling via Peltier device. Measurements were carried out under air in a 2θ range of 7 to 145° with a step size of 0.013° and a total scan time of 1 h. In situ high temperature XRD was realized by using an Anton Paar X-ray reaction chamber XRK900 (Anton Paar GmbH, Graz, Austria). Measurements were car-

ried out under a vacuum of 0.02 mbar in a 2θ range of 7 to 110° with a step size of 0.013° and a total scan time of 1 or 2 h. The temperature was varied in 25 or 50 K steps with a heating rate of 10 K/min up to a temperature of 600 °C.

Interpretation of the XRD data was achieved via the Rietveld method using TOPAS 5.[36–38] Crystallographic structure and microstructure were refined, while instrumental line broadening was included in a fundamental parameters approach.[39] The mean crystallite size <*L*> was calculated at the mean volume weighted column height derived from the integral breadth. The background of standard measurements was fitted by a Chebyshev polynomial function of 15th degree. The background of in situ high temperature measurements was fitted by a 1/*x*-function together with a Chebyshev polynomial function of 5th degree and two additional hat functions to correct the specific background profile present in all measurements. Crystal structure data were obtained from the crystallography open database (COD) and the inorganic crystal structure database (ICSD).[40,41]

FT-IR spectra were recorded on a Bruker Vertex 70 IR spectrometer (Bruker, Karlsruhe, Germany) in attenuated total reflection mode under ambient conditions. Spectra were recorded from 4000 to 400 cm^{-1} with a resolution of 4 cm^{-1} and 40 scans per spectrum.

Dynamic scanning calorimetry (DSC) was conducted with a Netzsch Phoenix 204 F1 (NETZSCH-Gerätebau GmbH, Selb, Germany). Measurements were carried out in aluminum crucibles under pure nitrogen and in a temperature range from –50 °C to 100 °C with a heating rate of 10 K/min.

Acknowledgments

We would like to thank Christina Odenwald for recording the SEM photographs.

Keywords: Solid-state reactions · Phase transitions · Reactive milling · Rietveld refinement · Structure elucidation

[1] M. M. Thackeray, *J. Am. Ceram. Soc.* **2004**, *82*, 3347–3354.
[2] C. Daniel, D. Mohanty, J. Li, D. L. Wood, *AIP Conf. Proc.* **2014**, *1597*, 26–43.
[3] D. G. Wickham, W. J. Croft, *J. Phys. Chem. Solids* **1958**, *7*, 351–360.
[4] M. M. Thackeray, W. I. F. David, P. G. Bruce, J. B. Goodenough, *Mater. Res. Bull.* **1983**, *18*, 461–472.
[5] N. Nitta, F. Wu, J. T. Lee, G. Yushin, *Mater. Today* **2015**, *18*, 252–264.
[6] Y.-M. Hon, K.-Z. Fung, M.-H. Hon, *J. Ceram. Soc. Jpn.* **2000**, *108*, 462–468.
[7] Y. Hon, S. Lin, K. Fung, M. Hon, *J. Eur. Ceram. Soc.* **2002**, *22*, 653–660.
[8] C. H. Lu, S. K. Saha, *J. Sol-Gel Sci. Technol.* **2001**, *20*, 27–34.
[9] X. Li, F. Cheng, B. Guo, J. Chen, *J. Phys. Chem. B* **2005**, *109*, 14017–14024.
[10] S. L. James, C. J. Adams, C. Bolm, D. Braga, P. Collier, T. Friić, F. Grepioni, K. D. M. Harris, G. Hyett, W. Jones, et al., *Chem. Soc. Rev.* **2012**, *41*, 413–447.
[11] N. V. Kosova, N. F. Uvarov, E. T. Devyatkina, E. G. Avvakumov, *Solid State Ionics* **2000**, *135*, 107–114.
[12] H.-J. Choi, K.-M. Lee, G.-H. Kim, J.-G. Lee, *J. Am. Ceram. Soc.* **2001**, *84*, 242–244.
[13] N. V. Kosova, E. T. Devyatkina, S. G. Kozlova, *J. Power Sources* **2001**, *97–98*, 406–411.
[14] S.-H. Kang, J. B. Goodenough, L. K. Rabenberg, *Chem. Mater.* **2001**, *13*, 1758–1764.
[15] N. Kamarulzaman, R. Yusoff, N. Kamarudin, N. H. Shaari, N. A. Abdul Aziz, M. A. Bustam, N. Blagojevic, M. Elcombe, M. Blackford, M. Avdeev, et al., *J. Power Sources* **2009**, *188*, 274–280.
[16] K. Momma, F. Izumi, *J. Appl. Crystallogr.* **2011**, *44*, 1272–1276.
[17] H. Hayakawa, T. Takada, H. Enoki, E. Akiba, *J. Mater. Sci. Lett.* **1998**, *17*, 811–812.
[18] V. Massarotti, D. Capsoni, M. Bini, P. Scardi, M. Leoni, V. Baron, H. Berg, *J. Appl. Crystallogr.* **1999**, *32*, 1186–1189.
[19] J. Akimoto, Y. Takahashi, Y. Gotoh, S. Mizuta, *Chem. Mater.* **2000**, *12*, 3246–3248.
[20] K. Kodama, N. Igawa, S. I. Shamoto, K. Ikeda, H. Oshita, N. Kaneko, T. Otomo, K. Suzuya, *J. Phys. Soc. Jpn.* **2013**, *82*, 1–6.
[21] A. Paolone, A. Sacchetti, P. Postorino, R. Cantelli, A. Congeduti, G. Rousse, C. Masquelier, *Solid State Ionics* **2005**, *176*, 635–639.
[22] W. I. F. David, M. M. Thackeray, L. A. De Picciotto, J. B. Goodenough, *J. Solid State Chem.* **1987**, *67*, 316–323.
[23] P. Strobel, F. Le Cras, L. Seguin, M. Anne, J. M. Tarascon, *J. Solid State Chem.* **1998**, *135*, 132–139.
[24] H. P. Beck, M. Douiheche, R. Haberkorn, H. Kohlmann, *Solid State Sci.* **2006**, *8*, 64–70.
[25] R. Haberkorn, J. Bauer, G. Kickelbick, *Z. Anorg. Allg. Chem.* **2014**, *640*, 3197–3202.
[26] A. Fischer, C. Ney, G. Kickelbick, *Eur. J. Inorg. Chem.* **2013**, *2013*, 5701–5707.
[27] A. Betke, G. Kickelbick, *New J. Chem.* **2014**, *38*, 1264–1270.
[28] A. Betke, G. Kickelbick, *Inorganics* **2014**, *2*, 410.
[29] G. Guerrero, P. H. Mutin, A. Vioux, *Chem. Mater.* **2001**, *13*, 4367–4373.
[30] A. M. Botelho do Rego, A. M. Ferraria, J. El Beghdadi, F. Debontridder, P. Brogueira, R. Naaman, M. Rei Vilar, *Langmuir* **2005**, *21*, 8765–8773.
[31] M. D. Lane, P. R. Christensen, *J. Geophys. Res. Planets* **1997**, *102*, 25581–25592.
[32] B. H. Toby, *Powder Diffr.* **2006**, *21*, 67–70.
[33] P. W. Stephens, *J. Appl. Crystallogr.* **1999**, *32*, 281–289.
[34] M. M. Thackeray, M. F. Mansuetto, D. W. Dees, D. R. Vissers, *Mater. Res. Bull.* **1996**, *31*, 133–140.
[35] R. Perthel, H. Jahn, *Phys. status solidi* **1964**, *5*, 563–568.
[36] H. M. Rietveld, *Acta Crystallogr.* **1967**, *22*, 151–152.
[37] H. M. Rietveld, *J. Appl. Crystallogr.* **1969**, *2*, 65–71.
[38] *Topas 5*, Bruker AXS, Karlsruhe, Ger. **2014**.
[39] R. W. Cheary, A. A. Coelho, J. P. Cline, *J. Res. Natl. Inst. Stand. Technol.* **2004**, *109*, 1–25.
[40] S. Gražulis, D. Chateigner, R. T. Downs, A. F. T. Yokochi, M. Quirós, L. Lutterotti, E. Manakova, J. Butkus, P. Moeck, A. Le Bail, *J. Appl. Crystallogr.* **2009**, *42*, 726–729.
[41] A. Belsky, M. Hellenbrandt, V. L. Karen, P. Luksch, *Acta Crystallogr., Sect. B Struct. Sci.* **2002**, *58*, 364–369.

Received: September 2, 2019